

Article

Correlation between Microstructural Properties and Electric Parameters of Micro-Arc Oxidation Coatings on 5052 Aluminum Alloys with Improving Wear and Corrosion Resistance

Jhu-Lin You^{1,2} , Chin-Jou Chang³ and Shun-Yi Jian^{3,4,*}

¹ Department of Chemical & Materials Engineering, Chung Cheng Institute of Technology, National Defense University, Taoyuan 335, Taiwan; yolin1014001@gmail.com

² System Engineering and Technology Program, National Chiao Tung University, Hsinchu 300, Taiwan

³ Department of Material Engineering, Ming Chi University of Technology, New Taipei 24301, Taiwan; asd870911@gmail.com

⁴ Center for Plasma and Thin Film Technologies, Ming Chi University of Technology, New Taipei 243303, Taiwan

* Correspondence: syjian@mail.mcut.edu.tw; Tel.: +886-2-29089899; Fax: +886-2-29084091

Abstract: Aluminum (Al) alloys are lightweight and machinable and have been widely used in industrial applications, particularly the formation of complex mechanical parts. However, the 5052 Al alloy frequently encounters problems like corrosion and wear during its service life, significantly impacting the equipment's longevity. This study investigated the effects of pulse voltage (320 to 400 V) and frequency (50 to 200 Hz) on the growth and surface morphology of 5052 Al alloy films formed through micro-arc oxidation (MAO) to improve their corrosion and wear resistance while maintaining a surface roughness of less than 1 μm . The results indicate that higher operating voltages and frequencies correlated with increased thickness in the resulting ceramic oxide films formed using MAO. In addition, as the pulse frequency increased, the distribution of the holes became more uniform across the surface. We examined the surface and cross-sectional morphology, as well as the thickness of the MAO coatings, through scanning electron microscopy (SEM). The corrosion and wear resistance of the MAO coatings formed under different electrical parameters were analyzed using electrochemical corrosion tests and scratch tests. The MAO coatings produced at 400 V and 200 Hz were the thickest, at approximately 4.8 μm , and demonstrated superior corrosion and wear resistance. These coatings demonstrate significantly reduced wear width, highlighting their exceptional resistance to corrosion and wear. Hole cracking occurred only above the top layer of the coating and not beneath the mid-layer, which protected the substrate from damage due to the direct passage of Cl ions through the holes.

Keywords: micro-arc oxidation (MAO); aluminum alloy; electrical parameters; electrochemical impedance spectroscopy; microstructure



Citation: You, J.-L.; Chang, C.-J.; Jian, S.-Y. Correlation between Microstructural Properties and Electric Parameters of Micro-Arc Oxidation Coatings on 5052 Aluminum Alloys with Improving Wear and Corrosion Resistance. *Coatings* **2023**, *13*, 1874. <https://doi.org/10.3390/coatings13111874>

Academic Editor: Philipp Vladimirovich Kiryukhantsev-Korneev

Received: 7 October 2023

Revised: 28 October 2023

Accepted: 30 October 2023

Published: 31 October 2023



Copyright: © 2023 by the authors. Licensee MDPI, Basel, Switzerland. This article is an open access article distributed under the terms and conditions of the Creative Commons Attribution (CC BY) license (<https://creativecommons.org/licenses/by/4.0/>).

1. Introduction

Light metals and their alloys are widely used as materials for substrates, housings, or mechanical components. Among these metals and alloys, Aluminum (Al) and its alloys are the most commonly used because they offer advantages such as high specific strength, lower weight, excellent processability, robust thermal conductivity, and compatibility with various surface treatments [1–4]. One such alloy, 5052 Al alloy, is a solid-solution-strengthened material that is used in electronic products and automobile bodies. Typically, the surface of 5052 Al alloy can spontaneously form a dense passivation film, which can provide protection. Unfortunately, the passivation film on the alloy surface is easily destroyed under harsh environmental conditions, including marine environments with high salt content, violent seawater erosion, temperature, and pressure. Thus, the 5052 Al alloy in the

service process will often cause parts corrosion, wear, and other issues, which seriously affect the service life of the equipment. In other words, 5052 alloy exhibits superior fatigue strength, ease of machining, corrosion resistance, and suitability for structural applications without the need for heat treatment [5,6]. However, as the demands for product strength and corrosion resistance continue to increase, effective strengthening mechanisms and surface treatments are indispensable to meet these requirements.

Al is also chemically active and naturally forms a thin oxide layer of approximately 5 nanometers that serves as a protective surface coating. However, this naturally occurring oxide layer lacks adequate thickness and uniformity, compromising its corrosion and wear resistance [7–10]. Therefore, an effective surface treatment is required to control the formation of the oxide layer and to improve the mechanical properties of Al alloys. Among available surface treatment methods, micro-arc oxidation (MAO), also called micro-plasma oxidation, stands out as a high-energy electrolytic surface modification technology that can be used to form ceramic oxide coatings in situ on valve metals and their alloys, thereby greatly improving wear resistance, hardness, and insulation [11–13]. MAO is mostly completed using low-concentration aqueous solutions of alkaline salts as electrolytes, indicating it does minimal environmental harm. MAO is a plasma-based process where a high-voltage electric field in an electrolyte creates micro-area arc discharges between an anode workpiece and a cathode plate. These discharges induce local high-temperature molten metal on the anode workpiece's substrate surface, resulting in oxidative sintering and ceramic film formation. MAO-derived ceramic film has a high micro-hardness and robust adhesion to substrates, and therefore inhibits anodic (oxidizing) currents and protects internal metal substrates from corrosion [14]. However, the MAO film formation process inevitably leads to microcracked and porous structures due to microdischarges and sparks that occur during the oxidation process [14–17]. Corrosive mediums can penetrate membrane and interface layers, causing substrate material corrosion [18,19]. Hence, optimizing the surface morphology and microstructure of MAO films is crucial for improving the corrosion resistance of Al alloys [20].

In this study, ceramic coatings on 5052 Al alloy were prepared using the MAO process to enable an investigation of how variations in breakdown voltage and frequency parameters affect the resulting microstructure. Limited research exists in the literature on the microstructure of 5052 Al alloy subjected to MAO, with the literature on optimizing the MAO process through adjustment of the aforementioned experimental parameters being particularly limited. Therefore, further research is required to fully characterize the oxide layer and determine the optimal conditions for the MAO process. In the present study, the thickness of the ceramic oxide film formed by MAO and the resulting surface roughness and corrosion resistance of the alloy were investigated. The surface morphology and cross-section microstructure of the MAO coatings were characterized by using a field-emission scanning electron microscope. Surface roughness is analyzed using a 3D optical profiler with the MountainsMap Imaging Topography software system (version 8.2). We also conducted electrochemical impedance spectroscopy (EIS) analysis with an electrochemical workstation, VersaSTAT 4, in a 3.5 wt.% NaCl solution as the corrosive medium. The abrasion resistance of the MAO coatings was tested using the Anton Paar RST³ scratch tester. Furthermore, the hydrophobicity of the coating surface was confirmed by measuring the contact angle between a water droplet and the surface microstructure using a contact angle instrument (Attension, Theta Lite, Gothenburg, Sweden). The enhanced hydrophilicity contributed to improved adhesion of the nanocomposite catalyst during subsequent chemical nickel or copper plating, resulting in coatings that exhibited increased corrosion and wear resistance on the alloys. The results of this study reveal the following: 1. The ceramic oxide film thickness exhibited a maximum thickness of nearly 5 μm . 2. The surface roughness (S_a) measured less than 1 μm . 3. The corrosion resistance and wear resistance of the manufactured substrates outperformed those of the original 5052 Al alloy substrates, providing significant advantages for the electronics, automotive bodies, and aerospace industries.

2. Materials and Methods

2.1. Material Preparation and MAO

Rectangular specimens ($100 \times 100 \times 2 \text{ mm}^3$) of 5052 Al alloy were used as substrates for the MAO process. The nominal chemical composition of this alloy, expressed in mass fractions, comprised 0.40% Fe, 0.15%–0.35% Cr, 0.10% Mn, 2.20%–2.80% Mg, and 0.10% Zr, with the remainder being Al. Prior to the MAO treatment, the oxide film on the surface of the specimens was removed through immersion in a 1 M NaOH aqueous solution for 2 min, then degreased with acetone and rinsed with distilled water. The MAO treatment setup included a potential adjustable DC pulse source, a 4.5 L stainless-steel vessel functioning as an electrolyte cell, a cooling system, and an agitation system. A schematic of the micro-arc oxidation setup is shown in Figure 1. The cooling system maintains the plating solution below 30°C during sample melting, ensuring uniform density in the entire MAO. Simultaneously, the stirring system homogenizes the plating solution temperature and evenly distributes ions within it. A stainless-steel container serves as the cathode, allowing more flexibility in sample sizing, while the 5052 Al alloy serves as the anode. The input voltage is varied between 320 V and 400 V in 40 V increments, and the frequency settings are 50 Hz, 100 Hz and 200 Hz. MAO was performed in an aqueous electrolyte by applying a pulsed DC electric field to the specimens. The electrolyte primarily consists of a silicate system, capable of producing both MgO and Mg_2SiO_4 , effectively enhancing the coating's corrosion resistance. The composition and concentration of the electrolytes are detailed in Table 1. After MAO treatment, the coated specimen was removed from the electrolyte, rinsed thoroughly with distilled water, and dried at room temperature. Table 2 lists the MAO operating parameters.

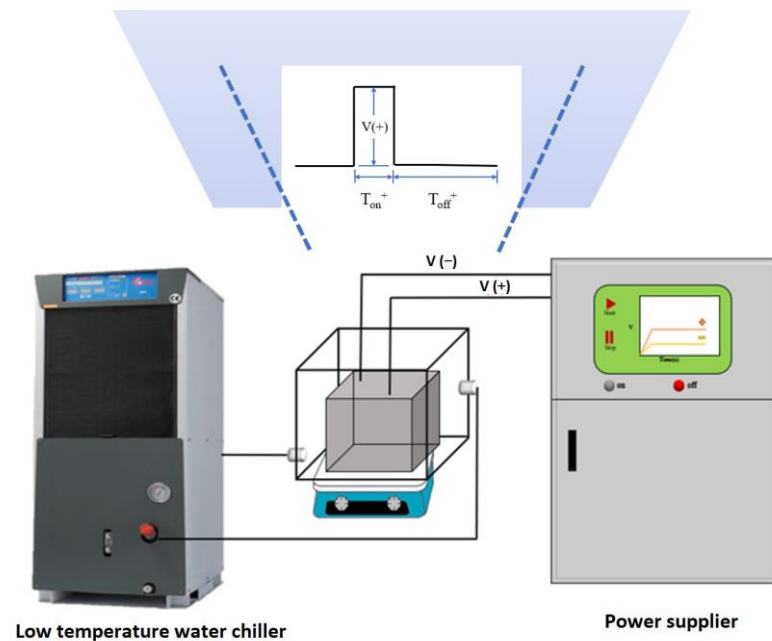


Figure 1. A schematic of the micro-arc oxidation setup.

Table 1. Composition and concentration of electrolytes for the MAO process.

Electrolytes Formula	1L
Na_2SiO_3	6 g
KOH	8 g
KF	8 g
$\text{Na}_2\text{WO}_4 \cdot 2\text{H}_2\text{O}$	0.56 g
$(\text{NaPO}_3)_6$	6 g

Table 2. MAO operating parameters.

Operating Parameter	Value
Initial temperature (°C)	below 10
Time (s)	360
DC field (V)	320, 360, 400
Frequency (Hz)	50, 100, 200

2.2. Coating Characterization

The surface morphology and cross-section microstructure of the MAO coatings were characterized by using a field emission scanning electron microscope (SEM; JEOL JSM-7610Fplus, JEOL Ltd., Tokyo, Japan) and a focused ion beam chamber (Hitachi NX2000, Tokyo, Japan). The thickness of the MAO coatings was further measured using cross-sectional SEM images. The surface roughness of MAO coatings was measured using a 3D surface measurement instrument (Chroma, 3D Optical Profiler Model 7503, Glasgow, UK) with a scanning area of $200\ \mu\text{m} \times 200\ \mu\text{m}$. MountainsMap Imaging Topography (Glasgow, UK, version 8.2) was used to analyze the surface roughness of the specimens. The phase structure of the MAO coatings was evaluated using an X-ray diffractometer (XRD; PANalytical x'pert pro, Malvern Panalytical, Malvern, UK). The electrochemical impedance spectroscopy (EIS) was analyzed using an electrochemical workstation VersaSTAT 4 (AMETEK Scientific Instruments, Berwyn, PA, USA). The potentiodynamic polarization curve test was evaluated using a three-electrode system. A saturated calomel electrode was used as a reference electrode (Counter Electrode, CE), a platinum plate functioned as the counter electrode (Saturated Calomel Electrode, SCE), the test sample as the working electrode (Working Electrode, WE), and a 3.5 wt.% NaCl solution as the corrosive medium. In the corrosion test, specimens with an area of $1.0\ \text{cm}^2$ were immersed in a 3.5 wt.% NaCl solution at room temperature. All samples will be stabilized at open circuit potential (OCP) for 1200 s prior to electrochemical measurement. The scan rate for the scan range used an OCP from -0.2 to $0.4\ \text{V}$ and the potentiodynamic polarization curve test was $0.005\ \text{V/s}$. To further assess surface hydrophobicity after coating, the apparent contact angle of the deionized water droplets on each sample was measured at room temperature using a contact angle instrument (Attension, Theta Lite, Espoo, Finland). Both the standard deviations and the mean values for the contact angles were determined by using more than five measurements obtained at different positions on each specimen. The abrasion resistance of the MAO coatings was tested using a scratch tester (Anton Paar RST³, Anton Paar, Graz, Austria) with the following operating parameters: a normal load of $0.5\text{--}30\ \text{N}$, length of $5\ \text{mm}$, and vibration frequency of $50.0\ \text{Hz}$ (speed of $10\ \text{N/s}$). After scratch tests, the wear tracks of the samples were observed using SEM.

3. Results and Discussion

3.1. Morphology of Ceramic Coating

The SEM micrographs of the surface of the MAO-coated 5052 Al alloy at different voltages and frequencies are presented in Figure 2. The images reveal a profusion of microcracks and micropores, visible as dark spots, resembling a honeycomb pattern. These holes are high-voltage spark discharge channels formed by the ejection and then the rapid cooling of the Al_2O_3 at the interface between the substrate surface and the electrolyte, creating paths for the flow of corrosion media. The high-magnification micrographs indicate that when the pulsed DC field voltage increased from $320\ \text{V}$ to $400\ \text{V}$, the diameter of the discharge channels increased, but the number of discharge channels decreased slightly, as shown in Figure 3a–i. The structure of the holes also changed from island-like and linear to a slightly curved circular hole. In addition, increasing the pulse frequency led to a more uniform distribution of holes across the surface.

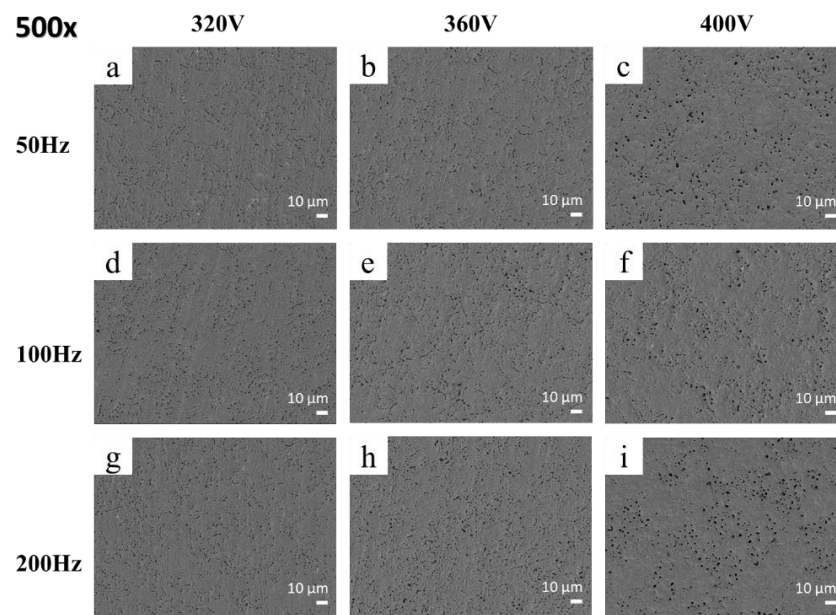


Figure 2. Surface SEM images of MAO-coated 5052 Al alloy at different voltages and frequencies: (a) 320 V, 50 Hz; (b) 360 V, 50 Hz; (c) 400 V, 50 Hz; (d) 320 V, 100 Hz; (e) 360 V, 100 Hz; (f) 400 V, 100 Hz; (g) 320 V, 200 Hz; (h) 360 V, 200 Hz; and (i) 400 V, 200 Hz.

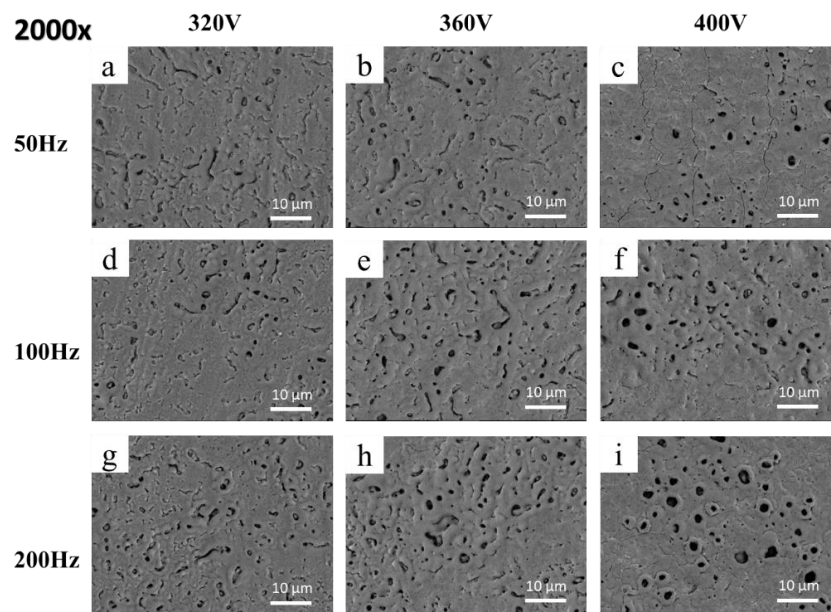


Figure 3. High-magnification surface SEM images of MAO-coated 5052 Al alloy at different voltages and frequencies: (a) 320 V, 50 Hz; (b) 360 V, 50 Hz; (c) 400 V, 50 Hz; (d) 320 V, 100 Hz; (e) 360 V, 100 Hz; (f) 400 V, 100 Hz; (g) 320 V, 200 Hz; (h) 360 V, 200 Hz; and (i) 400 V, 200 Hz.

Cross-sectional SEM images of the MAO coatings with different breakdown voltage and frequency parameters are presented in Figure 4. As is discernible from the images, different pulsed DC field voltages affected the performance of the MAO coatings. Figure 4a reveals that a low voltage setting of 320 V and a frequency of 50 Hz were insufficient to drive the growth of ceramic films. The oxide layer was scarcely observable at voltages of 320 V or lower. However, the thickness of the MAO coating increased significantly when the voltage and frequency were increased to 400 V and 200 Hz, as presented in Figure 4i. The growth of the coatings can be attributed to the oxidation of molten Al as it flows through the discharge channel [21–23]. The results indicate that an increase in

pulse voltage resulted in thicker film layers, which occurred because higher pulse voltages allow more electrical energy to reach the surface, thus enabling coating growth [24–26]. The thickness of MAO coating at different voltages and frequencies is summarized in Table 3. We further investigated the elemental distribution and content of the MAO films by EDS spectroscopy. The results of the EDS analysis are summarized in Table 4. Based on the EDS results, the MAO coating primarily consists of the elements O, Al, and Si, indicating that it is predominantly composed of aluminum oxide. In addition, the elemental oxygen content increases with higher voltage and frequency, indicating greater oxide formation in the MAO film. The SEM images also reveal a distinct interface between the oxide layer and the substrate, indicating that the MAO coatings were continuous and tightly bonded to the substrate. Observations from the cross-sectional SEM images of the hole areas revealed that the holes did not penetrate through the substrate at either low or high voltages, and the densification of the coatings did not decrease as the voltage increased. The MAO coatings produced at 400 V and 200 Hz (see Figure 4i) were dense and uniform compared with those formed at low pulse voltages and frequencies. The coating achieved at these optimal operating parameters exhibited the greatest thickness (approximately 4.8 μm), and the holes were cracked only above this layer and did not extend below its midpoint, which protected the substrate from direct Cl ion penetration. These findings indicate that pulse voltage and frequency are critical electrical parameters affecting the properties of MAO coatings, including their pore size and corrosion resistance.

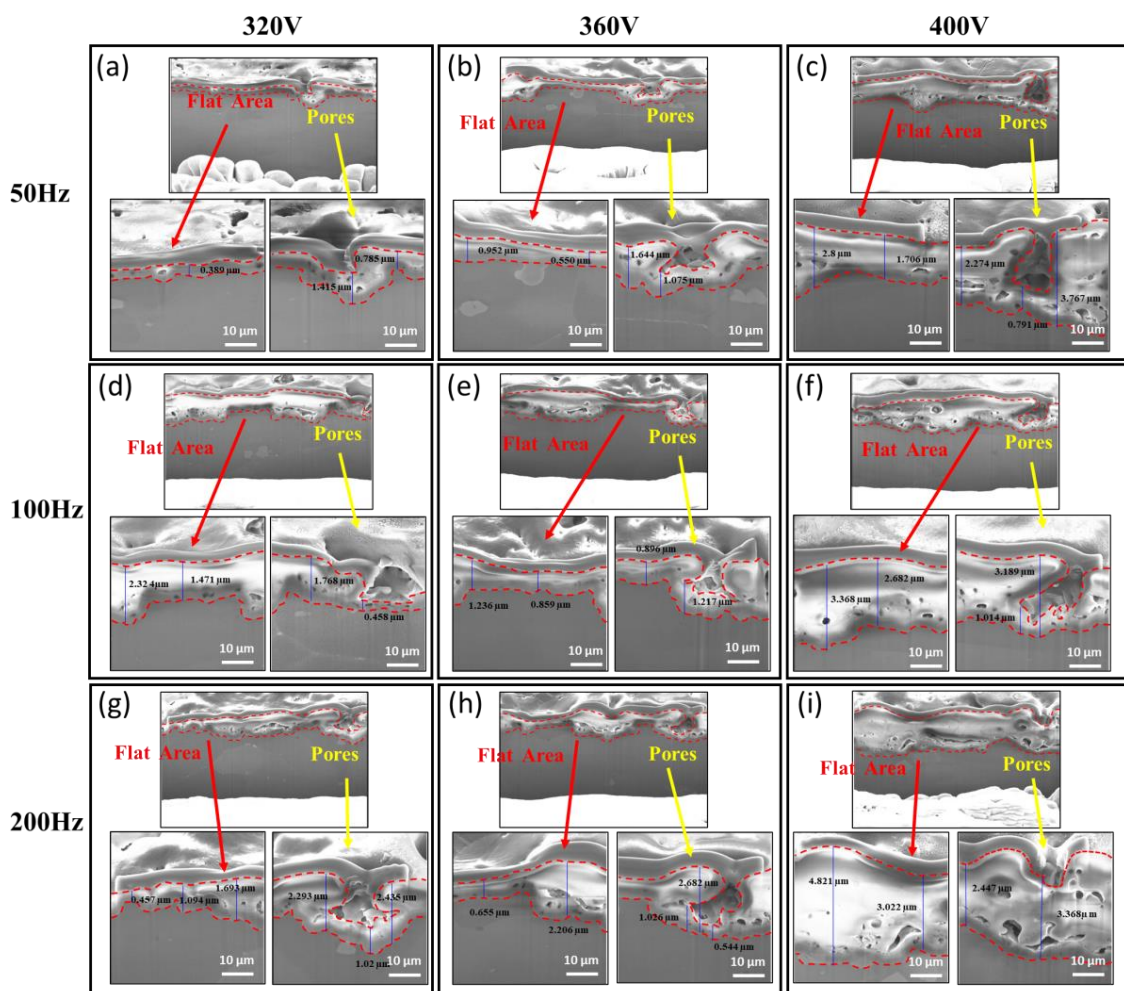


Figure 4. Cross-sectional SEM images of the coated 5052 Al alloy at different voltages and frequencies: (a) 320 V, 50 Hz; (b) 360 V, 50 Hz; (c) 400 V, 50 Hz; (d) 320 V, 100 Hz; (e) 360 V, 100 Hz; (f) 400 V, 100 Hz; (g) 320 V, 200 Hz; (h) 360 V, 200 Hz; and (i) 400 V, 200 Hz.

Table 3. The thickness of MAO coating at different voltages and frequencies.

Voltage (V)	320 V			360 V			400 V		
Frequency (Hz)	50 Hz	100 Hz	200 Hz	50 Hz	100 Hz	200 Hz	50 Hz	100 Hz	200 Hz
Thickness (μm)	0.86 ± 0.422	1.51 ± 0.678	1.50 ± 0.709	1.06 ± 0.391	1.05 ± 0.175	1.42 ± 0.862	2.27 ± 1.01	2.56 ± 0.929	3.41 ± 0.876

Table 4. EDS Analysis (at%) of Film.

Voltage	320 V			360 V			400 V		
Frequency	50 Hz	100 Hz	200 Hz	50 Hz	100 Hz	200 Hz	50 Hz	100 Hz	200 Hz
O	42.6	45.8	48.4	44.5	48.6	50.9	46.5	49.1	53.0
Al	48.7	45.5	42.9	47.2	42.5	40.0	46.7	43.4	39.2
Si	4.8	5.2	5.6	5.2	5.9	6.3	5.5	6.3	6.5
P	2.2	1.9	1.7	1.9	1.7	1.6	0	0	0
Mg	1.0	1.0	0.8	0.7	0.7	0.7	0.8	0.7	0.7
F	0.6	0.5	0.5	0.4	0.5	0.4	0.4	0.4	0.5
Na	0.1	0.1	0.1	0.1	0.1	0.1	0.1	0.1	0.1

3.2. Surface Roughness and Hydrophobic Analysis

Surface roughness is a crucial factor affecting the hydrophobic stability of a substrate surface. The surface roughness of the MAO coatings was measured using a three-dimensional (3D) surface measurement instrument, as depicted in Figure 5. As the pulse voltage and frequency increased, the value of Sa increased, as illustrated in Figure 6. The number of weak points susceptible to dielectric breakdown through microdischarges in the oxide coating diminished as pulse voltage and frequency increased. This resulted in a thicker coating, which caused a reduction in the number of micropores and an increase in the size of the micropores, which was attributed to a decrease in the number of discharge points capable of passing a higher pulse voltage and frequency. Consequently, as the MAO coating thickened, the pore size and surface roughness increased. According to the surface roughness results presented in Figure 6, the Sa of thicker films exceeded that of thinner films, aligning with the observations of relevant studies [24,27,28].

The contact behavior between water droplets and the coating surface was confirmed using hydrophobic analysis. As presented in Figure 7, a mild increase in hydrophilicity occurred when a higher pulse voltage and frequency were applied. The island-like linear structures became curved circular holes, which increased the surface area in contact with the water droplets and enhanced wettability. Despite this shift toward hydrophilicity, the coatings continued to exhibit hydrophobicity due to the increased surface roughness. Additionally, the slight increase in hydrophilicity helped improve the adhesion of the nanocomposite catalyst to the substrate during subsequent chemical nickel or copper plating, resulting in coated alloys that were more resistant to corrosion and wear [29–32]. Due to the hydrophilic nature of the surface, the nanocomposite catalyst particles enter into the pores of the MAO during the plating process, which results in the successful attachment of the catalyst to the surface. Thus, at the optimal operating parameters of 400 V and 200 Hz, a balance between thickness and hydrophilicity was achieved, which contributed to enhancing the corrosion resistance of the MAO coatings.

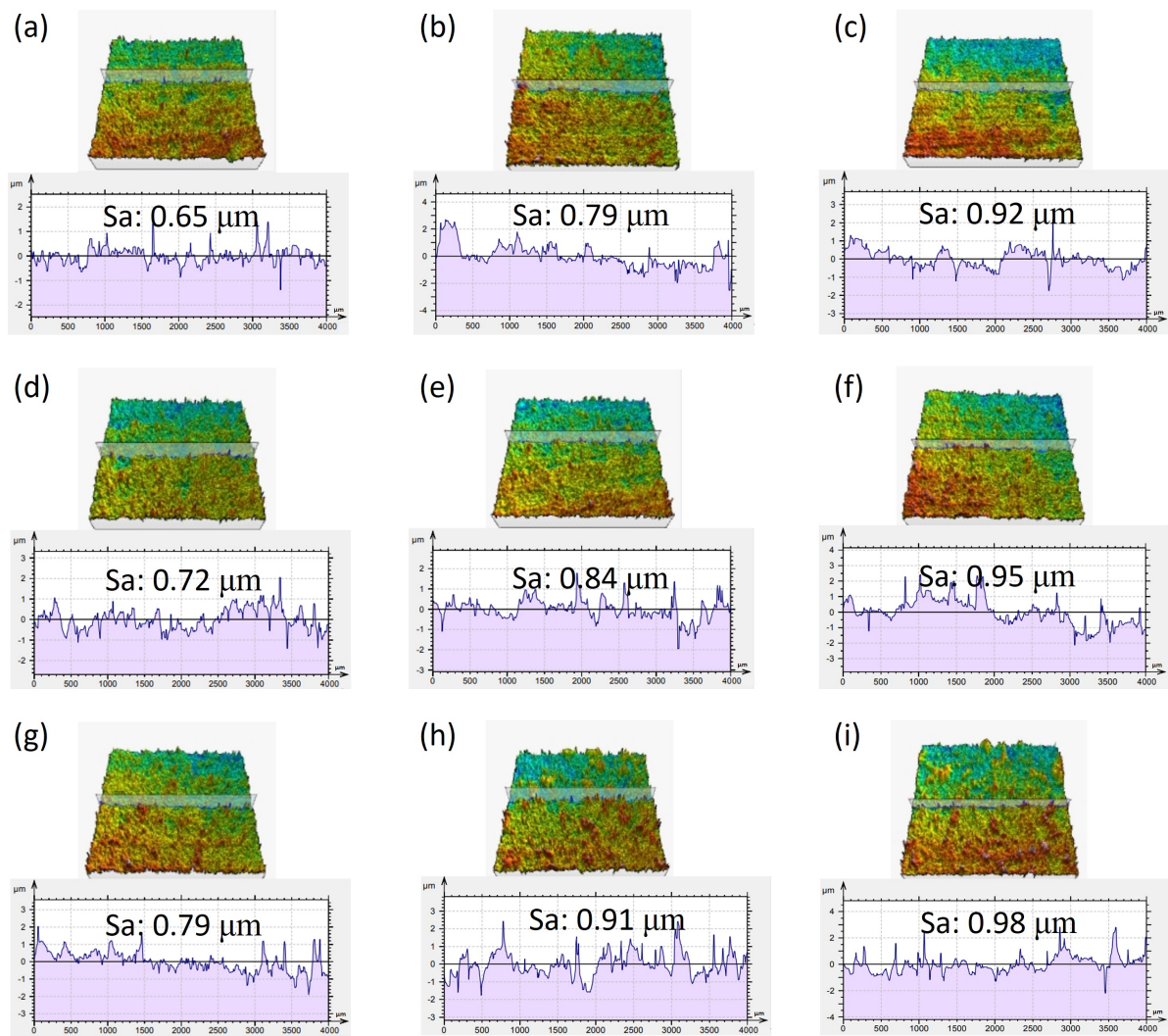


Figure 5. Surface roughness and 3D profile morphology of MAO coatings at different voltages and frequencies: (a) 320 V, 50 Hz; (b) 360 V, 50 Hz; (c) 400 V, 50 Hz; (d) 320 V, 100 Hz; (e) 360 V, 100 Hz; (f) 400 V, 100 Hz; (g) 320 V, 200 Hz; (h) 360 V, 200 Hz; and (i) 400 V, 200 Hz.

3.3. Phase Analysis

The crystalline phases in the oxide layers formed through the MAO process were characterized using XRD analysis, as depicted in Figure 8. The original 5052 Al alloy primarily consists of an α -Al phase and a small amount of Fe, Cr, and Mn, showing no phase variations in Mg [33]. In this study, the original 5052 Al alloy substrate exhibited Al peaks at 38° , 44° , 65° , and 78° , which were attributed to X-ray penetration through the substrate (see black line in Figure 8). The MAO-generated coatings comprise phases of Al, γ - Al_2O_3 , and α - Al_2O_3 (see red line in Figure 8). During the MAO process, different crystal structures (types) of Al_2O_3 were formed in the MAO film through a combination of chemical reactions with oxygen and electrochemical interactions with alkaline electrolytes. These reactions were influenced by factors such as the cooling rate and temperature. When the 5052 Al alloy was subjected to MAO in an alkaline electrolyte, a dense oxide film rapidly formed on the substrate surface. This rapid cooling rate mainly leads to the formation of γ - Al_2O_3 during solidification, whereas a slow cooling rate mainly leads to the conversion of molten Al_2O_3 to α - Al_2O_3 , with a small fraction of the γ - Al_2O_3 also converting to α - Al_2O_3 [34,35]. Relative to the other phases, α - Al_2O_3 has a hard texture and is insoluble in acids and alkalis. This property endows it with excellent corrosion resistance and electrical insulating properties, contributing to the overall corrosion resistance of MAO coatings.

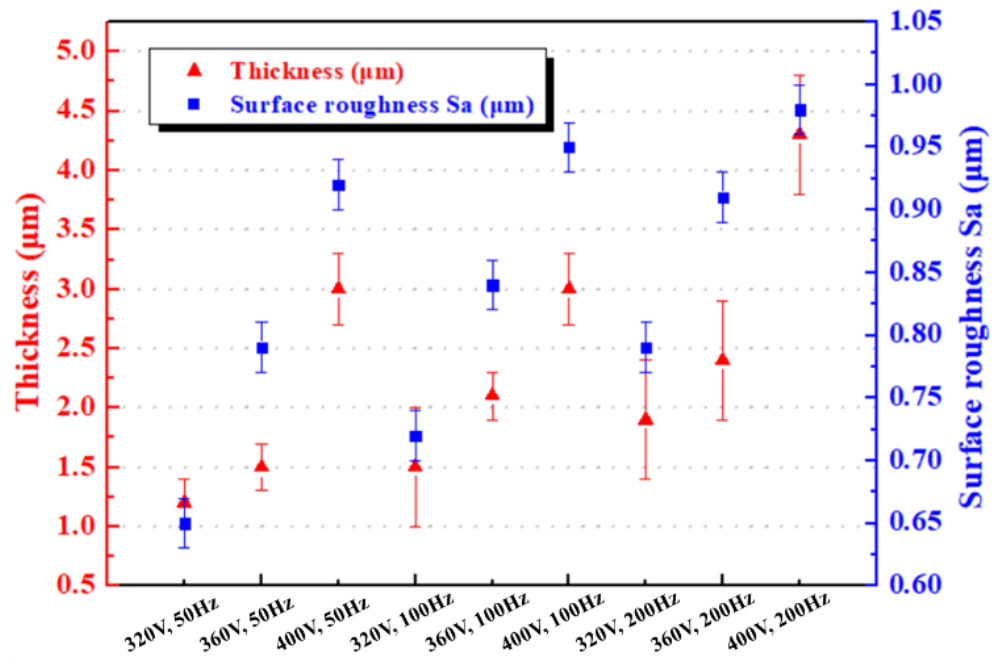


Figure 6. Surface roughness and thickness of MAO coatings at different voltages and frequencies.

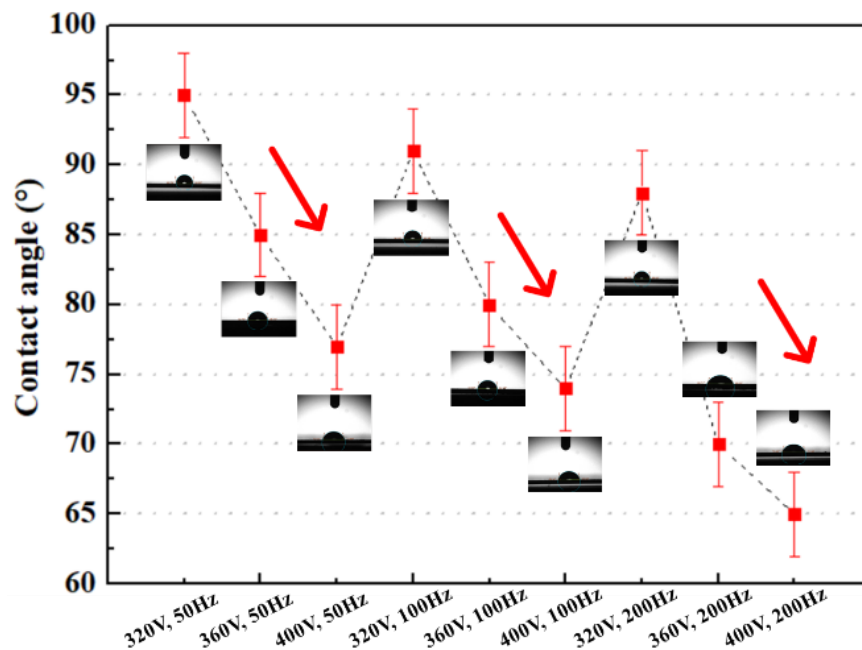


Figure 7. Contact angle of MAO coatings at different voltages and frequencies.

3.4. Electrochemical Corrosion Tests

MAO coatings improve corrosion resistance by providing a protective barrier against corrosive media. In our study, specific properties of MAO coatings, such as thickness and pore characteristics, significantly influence their shielding efficacy. EIS was employed to investigate the corrosion behavior of the samples. Figure 9a presents the EIS measurements for the samples immersed in a 3.5 wt% NaCl solution. An increase in corrosion resistance was observed when the frequency increased, keeping the voltage constant. Similarly, at a constant fixed frequency, the corrosion resistance enhanced significantly when the voltage value was increased. The most effective corrosion resistance was achieved at operating parameters of 400 V and 200 Hz. This is because as voltage and frequency increased, the thickness of the coating layer increased and the number of holes decreased, and the

distribution of the holes tended to be uniform. Although the diameter of the holes increased slightly, they did not penetrate the substrate. This effectively blocked the passage of Cl ions, thereby providing better long-term corrosion protection.

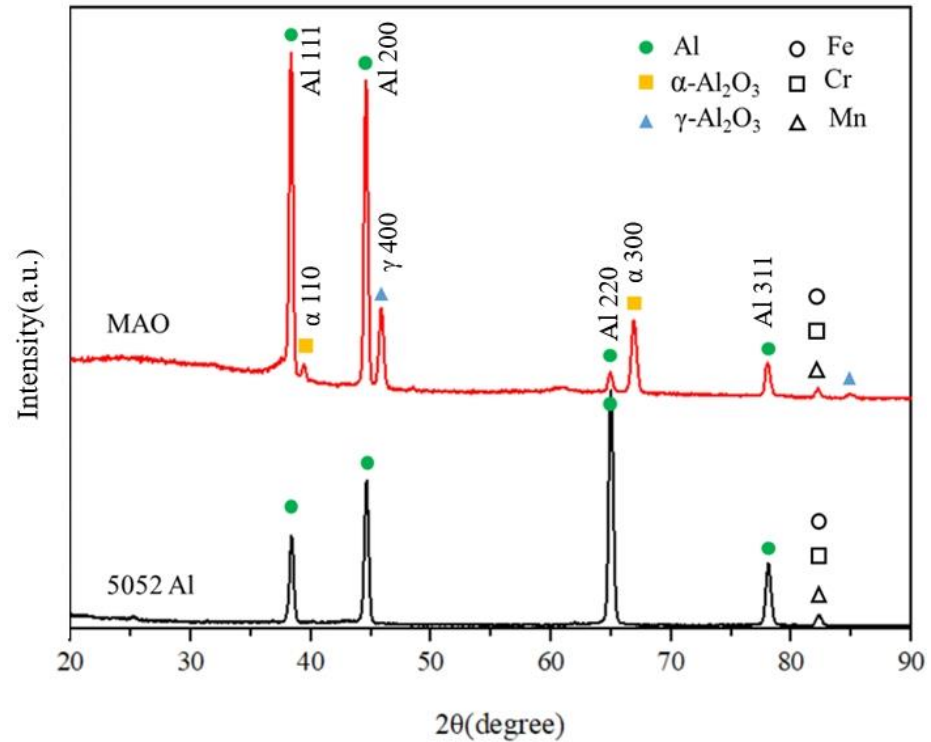


Figure 8. XRD patterns of oxide layers formed by the MAO process and the original 5052 Al alloy substrate.

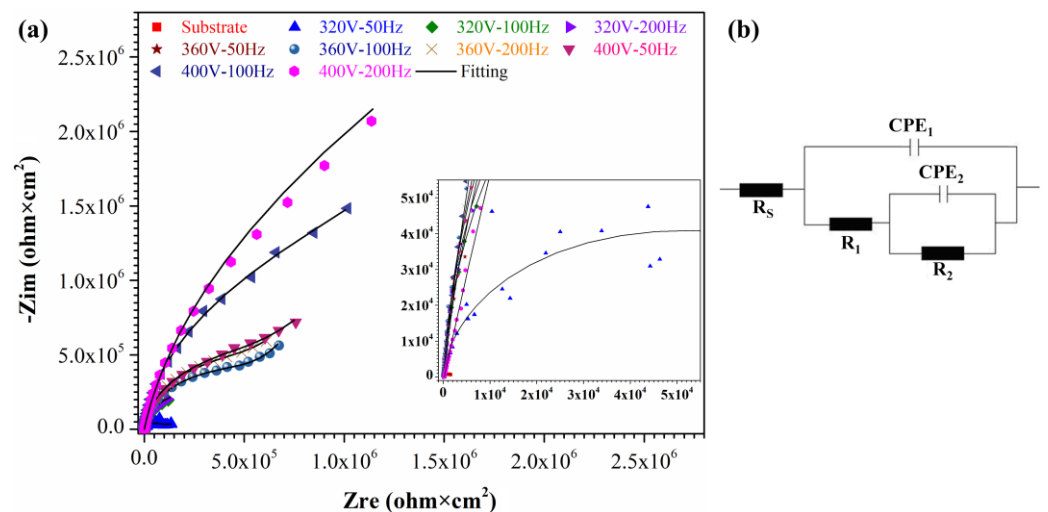


Figure 9. Electrochemical impedance spectrum as (a) Nyquist plots for the bare 5052 and the MAO coated 5052 samples; (b) equivalent circuit models for the simulation of the Nyquist plots.

The models chosen (Figure 9b) for the fitting of bare 5052 and the treated 5052 alloy: R_s is the resistance of the solution between reference and working electrodes. R_1 is the resistance of the coating and R_2 is the charge transfer resistance. The Constant Phase Element (CPE) is used instead of a capacitive element, which is parallel with R_1 and R_2 . The fitted results for the various 5052 plates are listed in Table 5. Results from the electrochemical corrosion test reveal that as voltage and frequency increase, both R_1 and R_2

impedance values exhibit an upward trend. This indicates the coating's ability to impede electron exchange at the surface of the 5052 Al alloy substrate, subsequently enhancing its resistance to corrosion. Moreover, the surface morphology and cross-sectional SEM images confirm that the 400 V-200 Hz coating is denser and thicker, showing no significant defects. This effectively prevents further diffusion or infiltration of the corrosive agent. In simple terms, the 400 V-200 Hz coating offers superior protection against corrosion in corrosive solutions.

The corrosion resistance of the MAO-coated 5052 Al alloy was conducted by the potentiodynamic polarization tests. Polarization curves of the bare 5052 Al alloy plate and the MAO-coated 5052 Al alloy plates in 3.5 wt.% NaCl solution is displayed in Figure 10. The current densities (i_{corr}) and corrosion potential (E_{corr}) values are presented in Table 6. E_{corr} represents the corrosion potential, which signifies the point at which the current density significantly increases, reflecting the behavior of metal dissolution until it reaches a critical value. i_{corr} , on the other hand, represents the corrosion rate. A more positive corrosion potential and lower corrosion current density indicate better corrosion resistance. It can be seen that the corrosion current density of MAO-coated 5052 Al alloy treated with higher pressure is lower than that of MAO-coated 5052 Al alloy treated with lower pressure. At the same voltage, MAO coatings on 5052 Al alloy treated at higher frequencies exhibit superior corrosion resistance compared to those treated at lower frequencies. Among them, the 400 V-200 Hz MAO-coated 5052 Al sample has the lowest i_{corr} (1.01×10^{-9} A/cm²), while the 320 V-50 Hz MAO-coated 5052 Al sample has the highest i_{corr} (6.65×10^{-6} A/cm²), as can be seen in Figure 10 and Table 6. Compared to the MAO-coated 5052 Al alloy, the untreated 5052 Al alloy (bare 5052 Al alloy) displayed the poorest corrosion resistance in a 3.5 wt.% NaCl solution, with a corrosion current density of i_{corr} 8.56×10^{-5} A/cm². After MAO treatment, a substantial reduction in corrosion current density was observed, leading to a significant improvement in corrosion resistance. The 400 V-200 Hz samples exhibited the highest corrosion resistance.

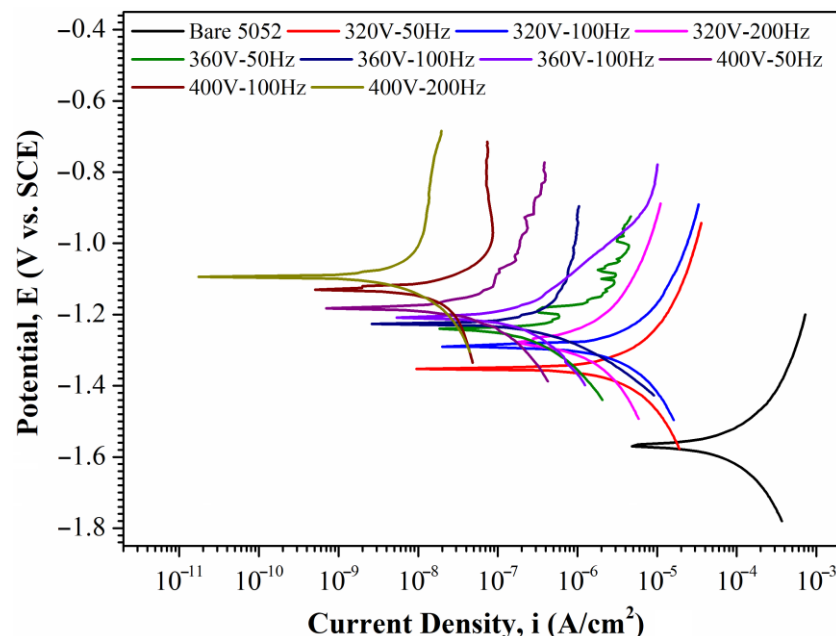


Figure 10. Polarization curves of the bare 5052 Al alloy plate and the MAO-coated 5052 Al alloy plates in 3.5 wt.% NaCl solution.

Table 5. Corrosion parameters and impedance for the bare 5052 and the MAO coated 5052 samples in 3.5% NaCl.

	Bare 5052	50 Hz	320 V 100 Hz	200 Hz	50 Hz	360 V 100 Hz	200 Hz	50 Hz	400 V 100 Hz	200 Hz
R_s (ohm·cm ²)	82.1	79.4	84.5	87.6	81.7	83.1	81.1	78.9	78.3	83.4
CPE_1 (s ⁿ ·μohm ⁻¹ ·cm ⁻²)	22.5	6.76×10^{-2}	4.73×10^{-2}	4.69×10^{-2}	5.86×10^{-2}	5.23×10^{-2}	4.82×10^{-2}	6.14×10^{-2}	6.17×10^{-2}	3.22×10^{-2}
CPE_1-n	0.84	0.71	0.97	0.98	0.98	0.97	0.97	0.95	0.95	0.99
R_1 (ohm·cm ²)	964	3.19×10^5	3.17×10^6	3.24×10^6	1.39×10^6	1.11×10^7	1.12×10^7	1.14×10^7	2.27×10^7	9.39×10^7
CPE_2 (s ⁿ ·μohm ⁻¹ ·cm ⁻²)	282	3.76	4.79	1.84	4.07	4.69	2.90	2.09	2.91	1.62
CPE_2-n	1	0.99	1	0.91	0.91	0.88	0.88	0.91	0.92	1
R_2 (ohm·cm ²)	697	6.35×10^4	4.92×10^5	4.98×10^5	3.15×10^5	1.14×10^6	2.15×10^6	2.29×10^6	3.37×10^6	3.91×10^6

Table 6. Results of potentiodynamic polarization tests of bare 5052 Al alloy and the MAO-coated 5052 Al alloy in 3.5 wt.% NaCl solution.

	Bare 5052	50 Hz	320 V 100 Hz	200 Hz	50 Hz	360 V 100 Hz	200 Hz	50 Hz	400 V 100 Hz	200 Hz
E_{corr} (V _{SCE})	-1.56	-1.35	-1.29	-1.27	-1.24	-1.23	-1.21	-1.18	-1.13	-1.10
i_{corr} (μA/cm ²)	85.6	6.65	2.88	8.89×10^{-1}	5.44×10^{-1}	1.28×10^{-2}	7.76×10^{-2}	4.76×10^{-2}	8.86×10^{-3}	1.01×10^{-3}

3.5. Scratch Testing

To further investigate the wear characteristics of the MAO-coated 5052 Al alloy at different voltages and frequencies, we evaluated the tribological properties under dry sliding conditions. Generally, the main forms of wear on the substrate are adhesive and abrasive wear, whereas the wear mechanism of the MAO coatings was mainly abrasive wear. The widths of the wear tracks on the MAO coatings were significantly reduced, which led to an improvement in wear resistance [5,36]. Figure 11 presents SEM images depicting the width of the wear tracks of different samples under dry sliding conditions. The MAO coatings formed at 320 V and 50 Hz exhibited much larger wear track widths compared with the other MAO-coated samples. These other samples were characterized by pronounced plow marks and scratches and an average width of 360.0 μm , indicative of severe plastic deformation and suboptimal wear resistance. These coatings were more susceptible to damage or spalling under external forces, owing to their irregular shapes and higher numbers of holes. Conversely, an increase in pulse voltage and frequency led to a decline in the number of holes, which also became more rounded and uniformly distributed. The wear width on the MAO coatings decreased significantly, indicating an improvement in wear resistance. Optimal wear resistance was achieved at operating parameters of 400 V and 200 Hz.

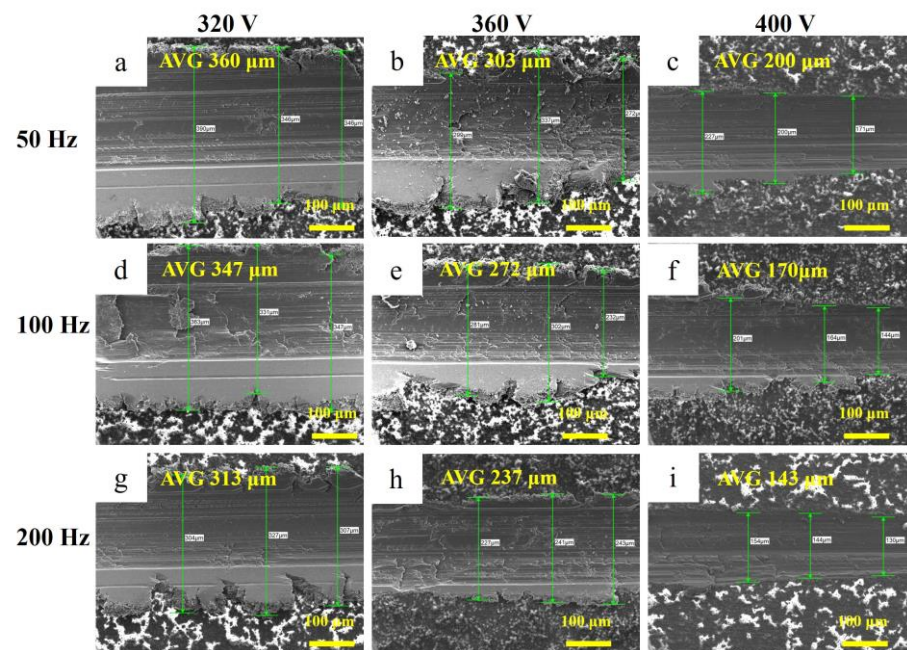


Figure 11. SEM images of the width of the wear tracks of different MAO-coated specimens under dry sliding conditions: (a) 320 V, 50 Hz; (b) 360 V, 50 Hz; (c) 400 V, 50 Hz; (d) 320 V, 100 Hz; (e) 360 V, 100 Hz; (f) 400 V, 100 Hz; (g) 320 V, 200 Hz; (h) 360 V, 200 Hz; and (i) 400 V, 200 Hz.

4. Conclusions

In this study, MAO ceramic coatings on 5052 Al alloy were fabricated using MAO under different breakdown voltage and frequency parameters. Pulse voltage and frequency were found to affect the morphology, thickness, hydrophilicity, and corrosion resistance of the coatings. When both pulse voltage and frequency increased, the coatings became thicker, the number of holes decreased, and the distribution of the pores tended to be uniform. Notably, at both low and high voltages, microcracks and micropores did not penetrate the substrate, and the coating densification remained stable regardless of voltage increases. The morphology and composition of the oxide coatings were investigated. During the MAO process, an increase in the pulse voltage of the discharge channel corresponded with a slight increase in the diameter of the discharge channels, leading to an increase in the roughness and hydrophilicity of the oxide coating. However, the coatings retained a

degree of hydrophobicity, and this balance between hydrophilicity and hydrophobicity made the somewhat rougher hydrophilic surface more suitable for subsequent chemical plating processes. XRD analysis revealed that the oxide coating was partially crystalline and consisted mainly of Al, γ -Al₂O₃, and α -Al₂O₃. The MAO coatings produced at 400 V and 200 Hz were the thickest, at approximately 4.8 μ m. Additionally, under these parameters, any cracking in the holes occurred only above the layer and not beneath its midpoint, thereby offering protection to the substrate against Cl ion penetration. This study provides valuable information regarding MAO processing of 5052 Al alloys and lays a solid foundation for future industrial applications.

Author Contributions: Methodology, J.-L.Y. and C.-J.C.; Investigation, C.-J.C.; Data curation, C.-J.C.; Writing—original draft, J.-L.Y. and S.-Y.J.; Writing—review & editing, S.-Y.J.; Funding acquisition, S.-Y.J. All authors have read and agreed to the published version of the manuscript.

Funding: This study is financially supported by the Ministry of Science and Technology of Taiwan, Republic of China, under Grant No. NSTC 111-2622-E-131-006. And the APC was funded by Ming Chi University of Technology (MCUT), New Taipei City, Taiwan.

Institutional Review Board Statement: Not applicable.

Informed Consent Statement: Not applicable.

Data Availability Statement: No new data were created or analyzed in this study.

Conflicts of Interest: The authors declare no conflict of interest.

References

1. Martin, J.H.; Yahata, B.D.; Hundley, J.M.; Mayer, J.A.; Schaedler, T.A.; Pollock, T.M. 3D printing of high-strength aluminium alloys. *Nature* **2017**, *549*, 365–369. [[CrossRef](#)] [[PubMed](#)]
2. Fang, J.; Mo, J.; Li, J. Microstructure difference of 5052 aluminum alloys under conventional drawing and electromagnetic pulse assisted incremental drawing. *Mater. Charact.* **2017**, *129*, 88–97. [[CrossRef](#)]
3. Venugopal, A.; Panda, R.; Manwatkar, S.; Sreekumar, K.; Krishna, L.R.; Sundararajan, G. Effect of micro arc oxidation treatment on localized corrosion behaviour of AA7075 aluminum alloy in 3.5% NaCl solution. *Trans. Nonferrous Met. Soc. China* **2012**, *22*, 700–710. [[CrossRef](#)]
4. Geanta, V.; Voiculescu, I.; Milosan, I.; Istrate, B.; Mates, I.M. Chemical Composition Influence on Microhardness, Microstructure and Phase Morphology of Al. *Rev. Chim.* **2018**, *69*, 798–801. [[CrossRef](#)]
5. Li, Y.; Zhang, D.; Qi, C.; Xue, Y.; Wan, Y.; Sun, H. Enhanced corrosion and tribocorrosion behavior of plasma electrolytic oxidized coatings on 5052 aluminum alloy with addition of pullulan to silicate electrolyte. *J. Alloys Compd.* **2023**, *960*, 170782. [[CrossRef](#)]
6. Rana, R.; Purohit, R.; Das, S. Reviews on the influences of alloying elements on the microstructure and mechanical properties of aluminum alloys and aluminum alloy composites. *Int. J. Sci. Res. Publ.* **2012**, *2*, 1–7.
7. Naeini, M.F.; Shariat, M.H.; Eizadjou, M. On the chloride-induced pitting of ultra fine grains 5052 aluminum alloy produced by accumulative roll bonding process. *J. Alloys Compd.* **2011**, *509*, 4696–4700. [[CrossRef](#)]
8. Tiringier, U.; Kovač, J.; Milošev, I. Effects of mechanical and chemical pre-treatments on the morphology and composition of surfaces of aluminium alloys 7075-T6 and 2024-T3. *Corros. Sci.* **2017**, *119*, 46–59. [[CrossRef](#)]
9. Wang, J.-H.; Du, M.-H.; Han, F.-Z.; Yang, J. Effects of the ratio of anodic and cathodic currents on the characteristics of micro-arc oxidation ceramic coatings on Al alloys. *Appl. Surf. Sci.* **2014**, *292*, 658–664. [[CrossRef](#)]
10. Liu, K.-P.; You, J.-L.; Jian, S.-Y.; Chang, Y.-H.; Tseng, C.C.; Ger, M.-D. Effect of electropolishing parameters of WE43 magnesium alloy on corrosion resistance of artificial plasma. *J. Mater. Res. Technol.* **2023**, *26*, 4989–5000. [[CrossRef](#)]
11. Chen, Q.; Li, W.; Ling, K.; Yang, R. Effect of Na₂WO₄ addition on formation mechanism and microstructure of micro-arc oxidation coating on Al-Ti double-layer composite plate. *Mater. Des.* **2020**, *190*, 108558. [[CrossRef](#)]
12. Arslan, E.; Totik, Y.; Demirci, E.; Vangolu, Y.; Alsaran, A.; Efeoglu, I. High temperature wear behavior of aluminum oxide layers produced by AC micro arc oxidation. *Surf. Coat. Technol.* **2009**, *204*, 829–833. [[CrossRef](#)]
13. Dehnavi, V.; Luan, B.L.; Shoosmith, D.W.; Liu, X.Y.; Rohani, S. Effect of duty cycle and applied current frequency on plasma electrolytic oxidation (PEO) coating growth behavior. *Surf. Coat. Technol.* **2013**, *226*, 100–107. [[CrossRef](#)]
14. Diggle, J. TC Downie and CW Goulding. *Anodic Oxide Film. Alum.* **1969**, *69*, 365–405.
15. Lv, X.; Zou, G.; Ling, K.; Yang, W.; Mo, Q.; Li, W. Tribological properties of MAO/MoS₂ self-lubricating composite coating by microarc oxidation and hydrothermal reaction. *Surf. Coat. Technol.* **2021**, *406*, 126630. [[CrossRef](#)]
16. Mu, M.; Liang, J.; Zhou, X.; Xiao, Q. One-step preparation of TiO₂/MoS₂ composite coating on Ti₆Al₄V alloy by plasma electrolytic oxidation and its tribological properties. *Surf. Coat. Technol.* **2013**, *214*, 124–130. [[CrossRef](#)]

17. Wang, Y.; Lu, D.; Wu, G.; Chen, K.; Wu, H.; Zhang, Q.; Yao, J. Effect of laser surface remelting pretreatment with different energy density on MAO bioceramic coating. *Surf. Coat. Technol.* **2020**, *393*, 125815. [[CrossRef](#)]
18. Sunilraj, S.; Blessto, B.; Sivaprasad, K.; Muthupandi, V. Microstructural and corrosion behavior of MAO coated 5052 aluminum alloy. *Mater. Today Proc.* **2021**, *41*, 1120–1124. [[CrossRef](#)]
19. Sobolev, A.; Kossenko, A.; Zinigrad, M.; Borodianskiy, K. Comparison of plasma electrolytic oxidation coatings on Al alloy created in aqueous solution and molten salt electrolytes. *Surf. Coat. Technol.* **2018**, *344*, 590–595. [[CrossRef](#)]
20. Raj, S.S.; Blessto, B.; Dhanasekaran, S.; Sivaprasad, K.; Muthupandi, V.; Sriramani, N. Combination of high strength and corrosion resistance in AA5052 alloy using cryorolling and micro arc oxidation. *Mater. Today Proc.* **2021**, *39*, 1738–1742.
21. Rehman, Z.U.; Shin, S.H.; Kaseem, M.; Uzair, M.; Koo, B.H. Towards a compact coating formed on Al6061 alloy in phosphate based electrolyte via two-step PEO process and K₂ZrF₆ additives. *Surf. Coat. Technol.* **2017**, *328*, 355–360. [[CrossRef](#)]
22. Rudnev, V. Micro- and nano-formations on the surface of plasma electrolytic oxide coatings on aluminum and titanium. *Surf. Coat. Technol.* **2013**, *235*, 134–143. [[CrossRef](#)]
23. Aliramezani, R.; Raeissi, K.; Santamaria, M.; Hakimizad, A. Characterization and properties of PEO coatings on 7075 Al alloy grown in alkaline silicate electrolyte containing KMnO₄ additive. *Surf. Coat. Technol.* **2017**, *329*, 250–261. [[CrossRef](#)]
24. Stojadinovic, S.; Vasilic, R.; Belca, I.; Petkovic, M.; Kasalica, B.; Nedic, Z.; Zekovic, L. Characterization of the plasma electrolytic oxidation of aluminium in sodium tungstate. *Corros. Sci.* **2010**, *52*, 3258–3265. [[CrossRef](#)]
25. Li, L.-H.; Kong, Y.-M.; Kim, H.-W.; Kim, Y.-W.; Kim, H.-E.; Heo, S.-J.; Koak, J.-Y. Improved biological performance of Ti implants due to surface modification by micro-arc oxidation. *Biomaterials* **2004**, *25*, 2867–2875. [[CrossRef](#)] [[PubMed](#)]
26. Lee, J.-L.; Jian, S.-Y.; Kuo, K.-n.; You, J.-L.; Lai, Y.-T. Effect of surface properties on corrosion resistance of ZK60 mg alloy microarc oxidation coating. *IEEE Trans. Plasma Sci.* **2019**, *47*, 1172–1180. [[CrossRef](#)]
27. Liu, S.; Chen, J.; Zhang, D.; Wang, Y.; He, Z.; Guo, P. Properties of micro-arc oxidation coatings on 5052 Al alloy sealed by SiO₂ nanoparticles. *Coatings* **2022**, *12*, 373. [[CrossRef](#)]
28. Yue, Y.; Hua, W. Effect of current density on corrosion resistance of micro-arc oxide coatings on magnesium alloy. *Trans. Nonferrous Met. Soc. China* **2010**, *20*, s688–s692.
29. Wang, Y.; Guan, L.; He, Z.; Zhang, S.; Singh, H.; Hayat, M.D.; Yao, C. Influence of pretreatments on physicochemical properties of Ni-P coatings electrodeposited on aluminum alloy. *Mater. Des.* **2021**, *197*, 109233. [[CrossRef](#)]
30. You, J.-L.; Chen, Y.-S.; Chang, C.-P.; Wu, M.-Z.; Ger, M.-D. Utilizing a pH-responsive palladium nanocomposite to fabricate adhesion-enhanced and highly reliable copper coating on nylon 6 fabrics. *J. Mater. Res. Technol.* **2021**, *15*, 3983–3994. [[CrossRef](#)]
31. You, J.-L.; Chang, C.-P.; Youh, M.-J.; Wu, M.-Z.; Chen, Y.-S.; Ger, M.-D. A reliable method by utilizing thermo-responsive palladium nanocomposite for fabricating Nickel coating on nylon 6 fabrics. *Colloids Surf. A Physicochem. Eng. Asp.* **2022**, *655*, 130160. [[CrossRef](#)]
32. You, J.-L.; Chang, C.-P.; Pu, N.-W.; Chen, Y.-S.; Wang, L.-H.; Pan, K.-H.; Ger, M.-D. Electroless plating of a 5G copper antenna on polyimide patterned with laser-induced selective activation and curing of metal-organic catalyst. *Appl. Surf. Sci.* **2022**, *599*, 153990. [[CrossRef](#)]
33. Moustafa, E.B.; Mosleh, A.O. Effect of (Ti-B) modifier elements and FSP on 5052 aluminum alloy. *J. Alloys Compd.* **2020**, *823*, 153745. [[CrossRef](#)]
34. Mohammed, A.A.; Khodair, Z.T.; Khadom, A.A. Preparation and investigation of the structural properties of α -Al₂O₃ nanoparticles using the sol-gel method. *Chem. Data Collect.* **2020**, *29*, 100531. [[CrossRef](#)]
35. Tseng, C.-C.; Lee, J.-L.; Kuo, T.-H.; Kuo, S.-N.; Tseng, K.-H. The influence of sodium tungstate concentration and anodizing conditions on microarc oxidation (MAO) coatings for aluminum alloy. *Surf. Coat. Technol.* **2012**, *206*, 3437–3443. [[CrossRef](#)]
36. Yang, W.; Wu, S.; Xu, D.; Gao, W.; Yao, Y.; Guo, Q.; Chen, J. Preparation and performance of alumina ceramic coating doped with aluminum nitride by micro arc oxidation. *Ceram. Int.* **2020**, *46*, 17112–17116. [[CrossRef](#)]

Disclaimer/Publisher’s Note: The statements, opinions and data contained in all publications are solely those of the individual author(s) and contributor(s) and not of MDPI and/or the editor(s). MDPI and/or the editor(s) disclaim responsibility for any injury to people or property resulting from any ideas, methods, instructions or products referred to in the content.